Delft University of Technology

Hyperbolic origami-inspired folding of triply periodic minimal surface structures

Callens, Sebastien J.P.; Tümer, Nazlı; Zadpoor, Amir A.

Important note
To cite this publication, please use the final published version (if applicable).
Please check the document version above.

Hyperbolic origami-inspired folding of triply periodic minimal surface structures

Sebastien J.P. Callens*, Nazlı Tümer, Amir A. Zadpoor

Department of Biomechanical Engineering, Delft University of Technology (TU Delft), Mekelweg 2, 2628 CD Delft, The Netherlands

ABSTRACT

Origami-inspired folding methods present novel pathways to fabricate three-dimensional (3D) structures from 2D sheets. A key advantage of this approach is that planar printing and patterning processes could be used prior to folding, affording enhanced surface functionality to the folded structures. This is particularly useful for 3D lattices, possessing very large internal surface areas. While folding polyhedral strut-based lattices has already been demonstrated, more complex, curved sheet-based lattices have not yet been folded due to inherent developability constraints of conventional origami. Here, a novel folding strategy is presented to fold flat sheets into topologically complex cellular materials based on triply periodic minimal surfaces (TPMS), which are attractive geometries for many applications. The approach differs from traditional origami by employing material stretching to accommodate non-developability. Our method leverages the inherent hyperbolic symmetries of TPMS to assemble complex 3D structures from a net of self-foldable patches. We also demonstrate that attaching 3D-printed foldable frames to pre-strained elastomer sheets enables self-folding and self-guided minimal surface shape adaption upon release of the pre-strain. This approach effectively bridges the Euclidean nature of origami with the hyperbolic nature of TPMS, offering novel avenues in the 2D-to-3D fabrication paradigm and the design of architected materials with enhanced functionality.

1. Introduction

Stochastic sheet-based micro-architectures are ubiquitous in engineering and natural materials and appear in the form of foams, sponges, bone tissue, or at the interface of phase-separated materials [1]. Their periodic counterparts, being more tractable to study, have received widespread attention too, especially geometries based on triply periodic minimal surfaces (TPMS). Minimal surfaces are surfaces that locally minimize area and are defined to have vanishing mean curvature everywhere ($H = 0$), which gives rise to their saddle-shaped appearance (with Gaussian curvature $K \leq 0$). Triply periodic minimal surfaces form a special class of minimal surfaces that are bicontinuous and periodic in three directions, hence they extend infinitely and divide space into two continuous, intertwined labyrinths [1]. While mathematicians were the first to study TPMS following the seminal work of Schwarz [2], the frequent observations of TPMS morphologies in a wide range of natural systems [3], ranging from self-assembled lipids [4] to butterfly wing scales [5], has sparked the interest of other scientists as well. Indeed, the unique structure-property relationships offered by TPMS have con-

tributed toward development of highly efficient cellular solids. For example, TPMS-based structures have been shown to combine high yield stress, low elastic modulus, exceptionally high fatigue resistance, and bone-mimicking transport properties, making them an ideal group of bone substitutes [6–8] Other examples include photonic metamaterials [9], architected materials [10,11], or porous membrane structures [12]. The functionality of lattice structures in general, and TPMS-based solids in particular, could be vastly augmented with planar surface-functionalization processes. For instance, precisely controlled surface nanopatterns could enhance the optical [13], wetting [14], osteogenic [15], and antimicrobial [16] properties of surfaces, while planar printing/imprinting techniques enable integration of embedded electronics into materials [17]. The incorporation of surface-related functionalities is particularly attractive for TPMS structures, given their very large surface-to-volume ratios. However, most 3D lattice structures, especially those based on TPMS, can currently only be manufactured using 3D printing techniques, which are incompatible with the planar functionality-inducing processes. To circumvent this incompatibility between 3D printing and planar processes, an origami approach has recently been proposed [18], where periodic beam-based lattices were shown to be foldable from a flat starting state, thereby enabling surface functionalization prior to folding. However, given the hyperbolic, *i.e.* non-developable, nature

* Corresponding author.
E-mail address: s.j.p.callens@tudelft.nl (S.J.P. Callens).

of TPMS, such conventional origami techniques are inherently ill-equipped to tackle the problem of folding TPMS morphologies from a flat state [19]. Therefore, we introduce a fundamentally different approach that circumvents the developability constraint and enables the folding of hyperbolic minimal surface morphologies, by leveraging sheet stretching. Due to the requirement of sheet stretching, one could describe this folding method as "origomu", signifying the folding of stretchable rubber-like sheets ("ori" means folding, "gomu" means rubber), as opposed to origami, signifying the folding of non-stretchable paper-like materials. While computational tools and differential growth-based fabrication methods for the generation of non-developable geometries from flat surfaces have been developed in recent years [20–23], these approaches typically require complicated material programming and the resulting shapes are often restricted to topological disks. The folding method that we introduce in this paper enables the folding of topologically complex porous structures with minimal surface morphologies, while requiring very limited material programming. The rationale behind our approach consists of realizing curved minimal surface patches from a flat state, by combining rigid foldable frames with pre-strained elastomer sheets. Multiple of these foldable patches could then be connected together in a net and used as building blocks to fold a myriad of 3D TPMS-based architectures, ranging from single unit cells to larger assemblies consisting of multiple unit cells and 3D stackable minimal surface layers.

2. Results

2.1. Hyperbolic geometry of TPMS

Triply periodic minimal surfaces belong to the realm of hyperbolic geometry and arise from symmetry operations on fundamental patches. This idea of constructing a TPMS structure as a 3D puzzle using a single, saddle-shaped puzzle piece that is repeated throughout the structure is central to our approach. As a demonstrative example, the translational unit cell of the well-known Schwarz P surface (Fig. 1a), can be tiled by a fundamental asymmetric patch (*Flächenstück*) through two symmetry operations: mirror reflections about the plane lines of curvature, and two-fold (π) rotations about the straight lines. The resulting triangular tiling, with angles $\pi/2$, $\pi/4$, and $\pi/6$, is not compatible with the Euclidean plane E^2, but is a tiling of the hyperbolic plane $\mathbb{H}^2$ (it is the *246 tiling in orbifold notation [24]), as seen in the conformal Poincaré disk model (Fig. 1a). This illustrates the interesting feature that a portion of $\mathbb{H}^2$ can be embedded in 3D Euclidean space E^3 by wrapping it onto the periodic minimal surface (albeit with some curvature distortion), analogous to embedding E^2 in E^3 by wrapping it onto a cylinder [24,25]. Within the context of this paper, however, this intrinsic connection between $\mathbb{H}^2$ and E^3 underpins the inherent complexity of trying to unwrap TPMS to a flat state, *i.e.* E^2. The same minimal surface could be tiled with different patches (Fig. 1b), all constructed from some symmetry operations on the elementary asymmetric patch. Within the wealth of known, intersection-free TPMS and their respective surface patches, our approach covers those surfaces that could be tiled by straight-edged skew polygonal patches (homeomorphic to a disk). A necessary (but not sufficient) condition therefore is the existence of embedded straight lines in the TPMS, which are axes of two-fold rotation and form the "linear skeletal net" of the surface [26]. TPMS with embedded straight lines were termed by Fisher and Koch as "spanning minimal surfaces" [27], and they are necessarily also minimal balance surfaces (*i.e.* the two labyrinths on both sides of the surface are congruent) [28]. Our folding approach applies to those spanning minimal surfaces for which the generating patch is a surface spanning a skew polygon. This excludes certain TPMS such as the H surface, which does not

contain straight lines but cannot be tiled by skew polygonal patches [27], and the well-known Gyroid surface, which does not contain embedded straight lines at all [28] (see SI). The presented approach does, however, cover a range of other widely studied TPMS, four of which are included in this paper as examples (see Fig. 1c, tiled by skew polygon patches): the P surface, the D surface (adjoint to P), the CLP surface, and the C(P) surface (complementary to P).

2.2. Foldable minimal surface patches

The key to our origami approach is the rational design of skew polygonal patches that could be flattened. We achieve this by adding hinges at some of the vertices of the boundary frame while keeping the edge lengths constant, enabling a continuous folding of the frame from a skew polygon to a (simple) flat polygon. For a skew n-gon ($n \geq 4$), this approach requires $2 \leq k \leq n/2$ hinges at the vertices, while the other vertices are kept fixed. Since the internal angle sum of the skew polygons is smaller than that of simple flat polygons, *i.e.* $\sum_i \alpha_i \leq \pi(n-2)$, the internal angles at the hinge vertices must increase during the unfolding motion (Fig. 1d–g). Applying the Gauss-Bonnet theorem to the skew polygonal boundary frame indicates that the folded frame must enclose negative Gaussian curvature (see SI) [29]. Consequently, the folding/unfolding of the polygonal boundary frame necessitates a change in the Gaussian curvature of the surface spanning the frame that, according to Gauss' *Theorema Egregium*, can only be accommodated by an area distortion [30]. Indeed, flattening the saddle shaped patches requires the surface spanning the frame to stretch (see Section 4). In other words, the metric of the surface has to transition between a Euclidean (flat) metric and a non-Euclidean (saddle-shaped) metric. With conventional origami folding, this would not be possible and the folded structures would remain intrinsically flat (except for some discrete points of non-zero Gaussian curvature in some techniques [31]). In our folding approach, the required area distortion during folding is achieved by attaching rigid, foldable frames to a biaxially pre-strained elastomer sheet. The pre-strain in the flat sheet entails two key benefits: releasing the pre-strained sheet drives self-folding of the attached frame from the flat state to the folded state, and the remaining pre-strain in the sheet forces it to adopt a minimal surface shape, by the virtue of energy (or area) minimization. This is analogous to the famous demonstrations of minimal surface formation that are obtained when dipping 3D wireframes in a soap solution: the soap film adopts a minimum-energy minimal surface shape. The same principle has been employed to create physical models of minimal surfaces (before the advent of 3D printing) using stretched fabrics or polymer sheets [32,33], and as a means to actuate certain origami tessellations [34].

The four patches considered here and their folding kinematics are shown in Fig. 1d–g. The skew hexagonal frames for the P and D surfaces (Fig. 1d, e) are equilateral and equiangular, and are the Petrie polygons of the regular octahedron and the cube respectively. The P-patch is flattened to an equilateral triangle, and the D-patch to an equilateral hexagon with angles of $\pi/2$ and $5\pi/6$. This simple folding/unfolding kinematics entails a rotation of angle θ around three "creases" that connect the hinge vertices (the dotted lines). In the case of the hexagonal patch of the CLP surface (Fig. 1f), only two hinges are required, and, thus, one "crease". The patch can then be flattened to a rectangle with sides l and $2l$. Finally, the patch for the C(P) surface is a skew octagon with alternating angles of $\pi/2$ and $\pi/3$, which is flattened to a bow-tie shape with angles π, $\pi/3$, and $4\pi/3$. Contrary to the three other patches where the location of the hinge points remains fixed, the flattening of the C(P) patch requires in-plane sliding of the hinge points during the folding motion (see Section 4). The C(P) skew octagonal patch could be flattened into different shapes that do not require sliding hinges,
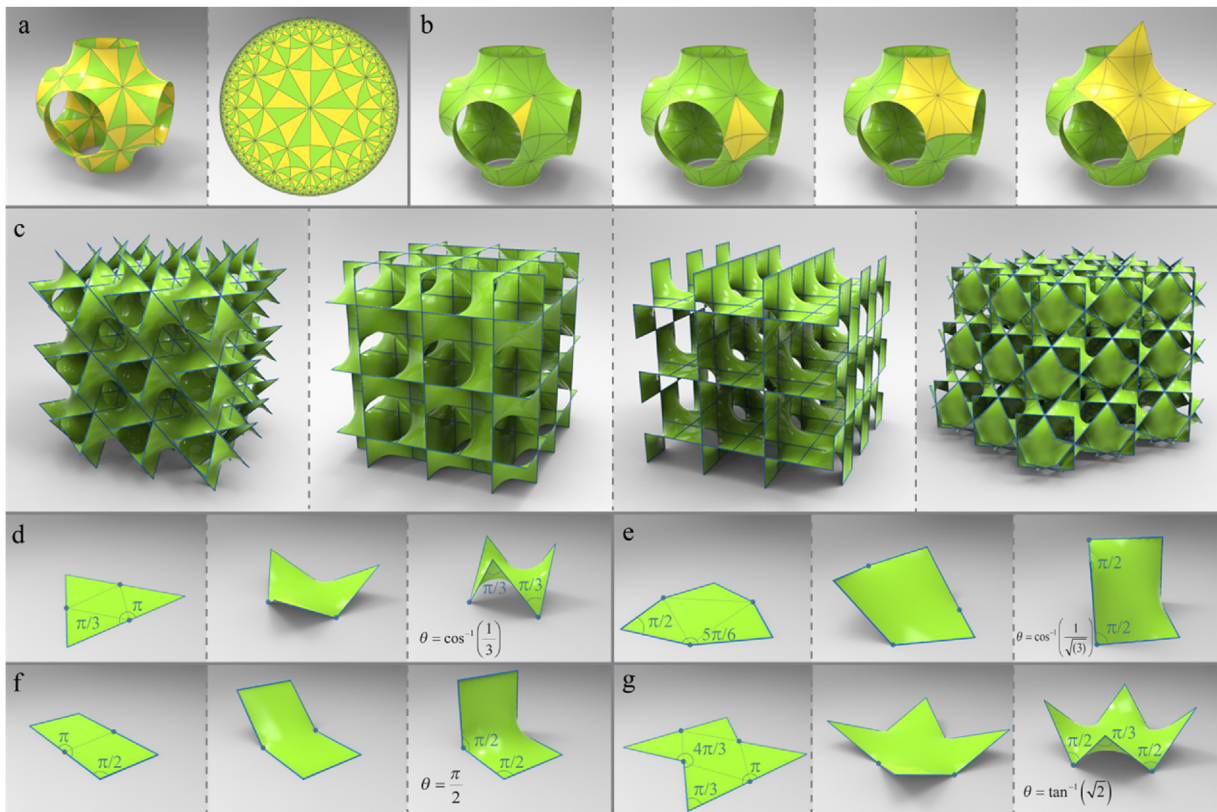
Fig. 1. Geometry of TPMS and patch folding. (a) A translational P unit cell decorated with the hyperbolic *246 tiling of the fundamental asymmetrical patch. (b) Alternative patches to tile the P surface, shown together with the conventional unit cell. (c) The four TPMS considered here. From left to right: P, D, CLP, and C(P) surface. (d) Folding kinematics for the straight-edged skew polygonal patches of the P, D, CLP, and C(P) surfaces, respectively.

but these alternative shapes are unfit for building an "overlap-free" 2D net that could be folded into 3D TPMS morphologies (see SI).

2.3. Patch connections and unit cell folding

Now that a suitable folding/unfolding approach for the minimal surface patches, *i.e.* the pieces of the 3D TPMS puzzle, has been obtained, the next key step is to connect patches together to build larger portions of the minimal surfaces. As such, we develop a foldable 2D "net" that results in a 3D portion of the TPMS once all patches have been folded. We identify two possible attachment strategies, namely edge-connections and vertex-connections. In the first type (Fig. 2a), two patches are connected by means of a π-rotation around their common edge $\boldsymbol{u}$, which is an inherent property of the straight lines embedded in minimal surfaces and justifies our focus on straight-edged skew polygonal patches. A consequence of this π-rotation is that the common edge remains coplanar with two adjacent edges $\boldsymbol{v_1}$ and $\boldsymbol{v_2}$, *i.e.* $\boldsymbol{u} \cdot (\boldsymbol{v_1} \times \boldsymbol{v_2}) = 0$, during the entire folding motion (Fig. 2a). The connection between both patches is therefore "rigid" and there is no need to actuate the folding of one patch relative to the other. The vertex-connection type attaches two patches at a vertex that is not a hinge point (Fig. 2b). A vertex-connection is established as a 2θ rotation about an axis $\boldsymbol{n}$ that is normal to the edges $\boldsymbol{u_1}$ and $\boldsymbol{v_1}$ meeting at the vertex, where $\theta = \cos^{-1}\left(\frac{\boldsymbol{u_1} \cdot \boldsymbol{v_1}}{\|\boldsymbol{u_1}\|\|\boldsymbol{v_1}\|}\right)$. In fact, this type of connection is the result of two consecutive edge-connections, *i.e.* a π-rotation over $\boldsymbol{v_1}$ followed by a π-rotation over $\boldsymbol{u_1}$ (Fig. 2b). Similar to the case of edge-connections, the edges $\boldsymbol{u_1}, \boldsymbol{v_1}, \boldsymbol{u_2},$ and $\boldsymbol{v_1}$ are coplanar, meaning that the vertex-connection is also rigid and can be physically realized without having to account for the relative motions between both patches at the connecting vertex. Experimenting with patch connections quickly reveals the most crucial challenge in our

folding strategy: avoiding overlaps in the 2D net. This challenge arises as a consequence of trying to confine the hyperbolic tiling of TPMS patches to the Euclidean plane. For example, the tiling with skew hexagons of the D surface (Fig. 2c), is a hyperbolic (6,4) tiling where four hexagons meet at every vertex. Attempting to achieve this with the flattened hexagonal patches leads to an overlapping 2D net, while the folded configuration is free of overlaps (Fig. 2c). This shows that it is not trivial to unwrap TPMS morphologies into 2D overlap-free nets. Our rational approach to overcome this challenge consists of first creating foldable, overlap-free nets for the TPMS unit cells, and using those unit cell nets as *prototiles* in the construction of overlap-free nets for larger structures. Thus, instead of assembling larger morphologies patch by patch, we propose to first define the net for a single translational unit cell and consequently connect those unit cell nets together to build larger structures. As shown in Fig. 2d–g, the translational unit cells for the P, D, CLP and C(P) surfaces respectively could all be folded from overlap-free 2D nets consisting entirely of vertex connections. In case of the P, D and CLP surfaces, the unit cell consists of 4 patches while the C(P) unit cell is constructed using 6 patches. A consequence (and advantage during physical realization) of using vertex-connections is that all patches fold in the same direction, which is not the case for edge-connections, causing the unit cell net to close in on itself, analogous to the folding of a paper cube. Except for the CLP unit cell net, the vertex-connected unit cell nets presented in Fig. 2 are not unique, *i.e.* different arrangements of vertex-connected patches could be generated that fold into the same translational unit cell. Examples of different nets that fold into the same translational unit cell are shown in Fig. S8 (see also SI). In general, the net for a unit cell consisting of n patches would need at most $n-1$ vertex-connections connecting two patches together. However, a net with fewer connections could be designed if more than two patches
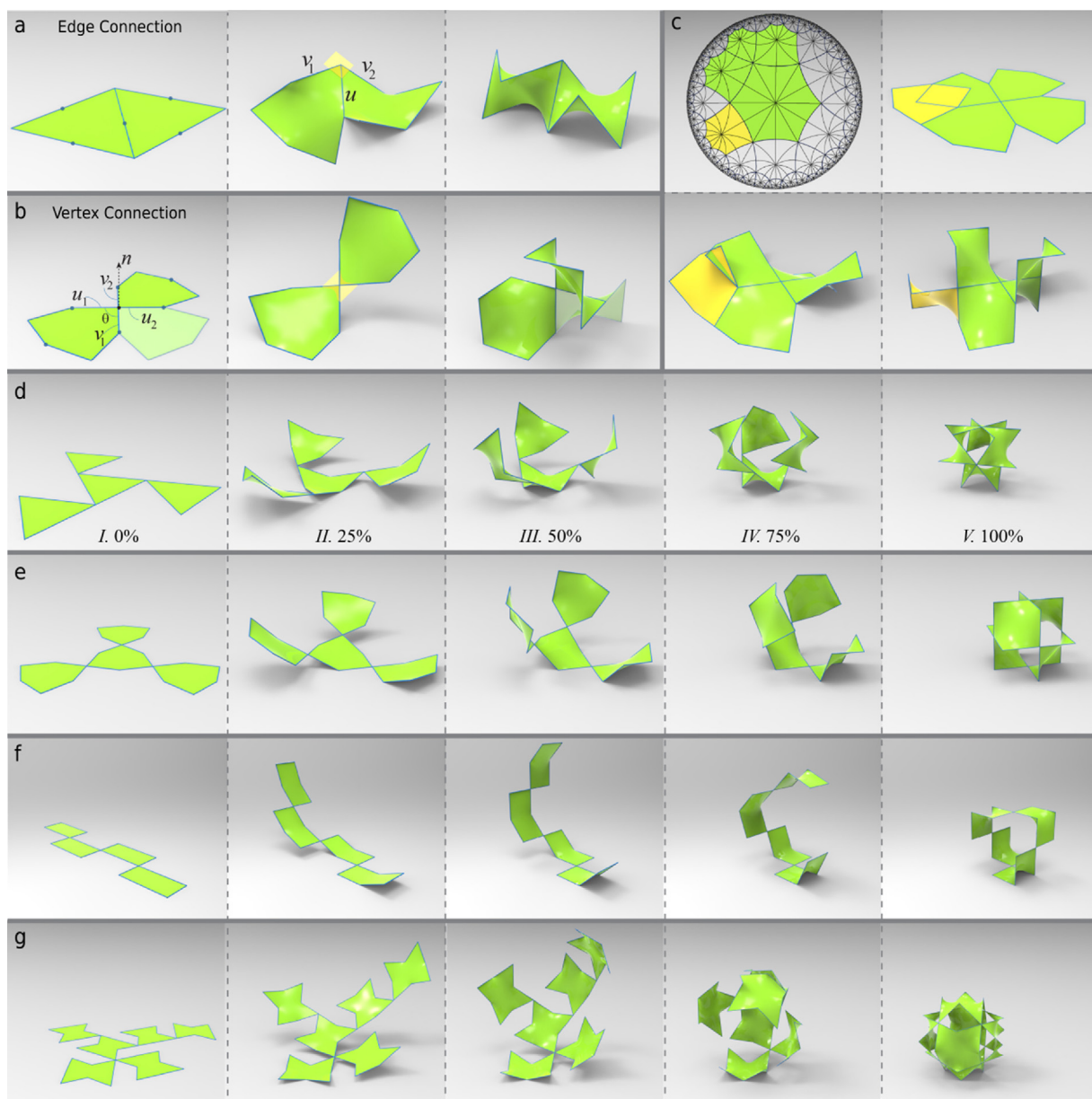
Fig. 2. Connecting patches. (a) The edge-connection of two P patches. (b) The vertex-connection of two D patches. A transparent patch indicates a patch that fits in between two vertex-connected patches. (c) When trying to conform the hyperbolic (6,4) tiling of the D surface to the flat plane, one frequently encounters overlaps in the 2D net. (d–g) The folding of TPMS unit cells consisting of vertex-connected patches.

could be attached together at the same vertex (*e.g.* in the case of the P and C(P) surfaces, see also SI). The same rationale to design nets for larger TPMS structures applies, independent of the choice of unit cell net. However, certain unit cell nets might be preferable in order to construct larger assemblies, as explained in the next section.

2.4. Multiple-unit cell assemblies

To establish folding of larger TPMS assemblies consisting of multiple unit cells, we connect the 2D nets of several unit cells together. This requires the use of edge-connections between the different unit cells, since further use of vertex connections would lead to overlaps in 3D, a consequence of the "closing" of the unit cells. To avoid overlaps in the 2D nets, however, not all edges are available for edge-connections. The admissible edges for the four unit cell nets considered here are highlighted in Fig. 3a. Only along these admissible edges, two unit cells can be connected without causing

overlaps in the 2D net. The admissible edges of a given unit cell net are those edges that lie on the edges of the convex polygon that defines the convex hull of the patch vertices (see Fig. S8). Thus an edge whose end points are vertices of the convex hull would be an admissible edge for edge-connections. All edges that are contained entirely within the convex hull (and not on the boundary) are inadmissible for edge-connections. A simple example of two connected P unit cells is provided in Fig. 3b, illustrating the opposite folding directions of both unit cells. Furthermore, Fig. 3b shows how connecting two units along one edge, *e.g.* u_1, may prohibit a connection along another edge, *e.g.* v_1, as this would otherwise lead to overlaps in 2D. The number of admissible edges varies depending on the chosen unit cell net. For example, some unit cell nets of the C(P) surface allow for only a single edge-connection, making them unsuitable to extend the 2D net beyond two unit cells (see Fig. S8 and SI). The net that is depicted in Figs. 2g and 3a, on the other hand, has six admissible edges (appearing in three pairs). Choosing
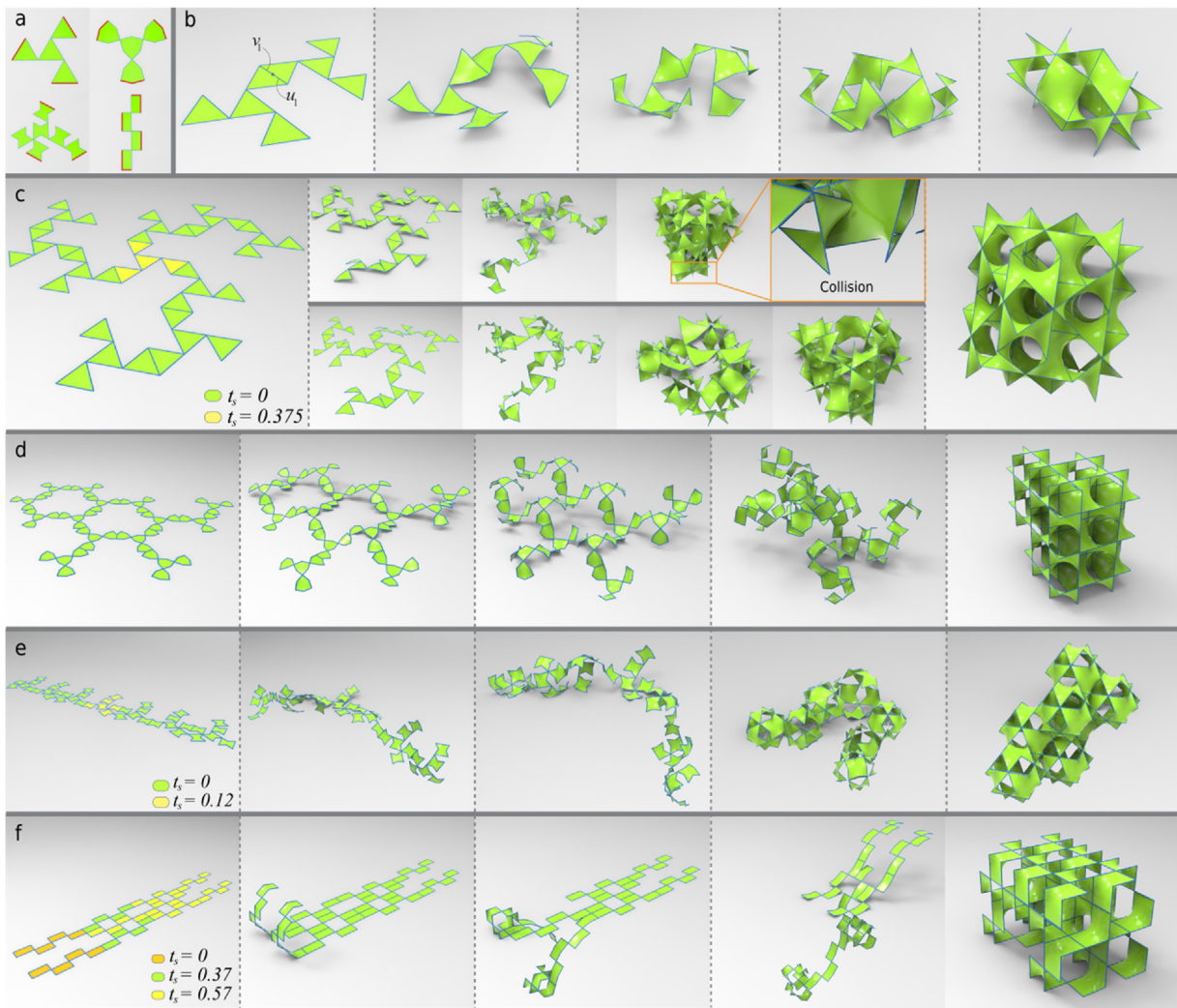
Fig. 3. Folding multiple-unit assemblies. (a) The unit cell edges that are available for edge-connections (highlighted in red) without causing overlaps in the 2D net. (b) Folding of two edge-connected P unit cells. (c) Folding of a 10-unit-cell net of the P surface without implementing sequential folding (top row), giving rise to collisions, and with sequential folding (bottom row), to avoid collisions. The yellow patch in the left pane starts folding with a delay relative to the other patches (fully folded configuration at $t = 1$). (d) Folding of a 14-unit-cell net of the D surface without requiring sequential folding. (e) The sequential folding of a 7-unit-cell net of the C(P) surface, with a folding delay applied to the central patch (yellow in the left pane). (f) Sequential folding of a 10-unit-cell assembly of the CLP surface, containing three separate folding starting times to avoid collisions. See SI for additional morphologies and SI_Movie1 through SI_Movie6. (For interpretation of the references to color in this figure legend, the reader is referred to the web version of this article.)

the latter unit cell net as a prototile would thus offer more freedom to construct a larger net, since it could connect to three other unit cells. To explore the folding of larger and more general TPMS morphologies, we constructed a computational tool that calculates the folding and the resulting 3D configuration of a user-defined input 2D net. Starting from a single unit cell, we extend the 2D net by adding more unit cells, without causing overlaps, and verify the resulting folding motion and the final 3D morphology. The underlying folding kinematics of our approach is surprisingly simple, since all folding information is captured in the kinematics of a single patch (assuming all patches fold simultaneously) and in the way the patches are connected together through vertex- and edge-connections (see Section 4). A large variety of 3D TPMS-based structures could be obtained without having to determine a separate folding strategy for each simply by varying the 2D arrangement of the patches (see SI). While still tractable for smaller structures, the relationship between a given 2D net and the resulting 3D structure becomes increasingly complex for larger structures with many patch connections, involving intricate folding motions and potentially overlapping patches in 3D that do not overlap in 2D, which are

detected in the tool by checking for duplicate sets of vertex coordinates. Using this explorative tool, a multitude of 2D nets could be designed to fold a wide range of complex minimal surface structures, some of which are shown in Fig. 3 and more can be found in the SI (*e.g.* minimal surface string-like morphologies or stackable layers). In Fig. 3c–f, the folding of multiple connected unit cells for the P, D, C(P), and CLP surfaces is illustrated (see SI_Movie1 to SI_Movie6). Due to the complex folding motions arising for such large structures, collisions during folding could occur, as shown in the top row of Fig. 3c for the folding of ten P unit cells. We demonstrate that sequential folding, *i.e.* temporal control over the folding motion, could alleviate this problem. As a simple example, a slight delay in the folding initiation of a centrally located unit cell in the nets of the P (Fig. 3c) and C(P) (Fig. 3e) morphologies is sufficient to enable collision-free folding, by maintaining adequate separation between the outwards extending arms. For the CLP example in Fig. 3f, three different starting moments are implemented to avoid collisions, a consequence of the high aspect ratio of the unit cell net, while the assembly of 14 D unit cells (Fig. 3d) did not require sequential folding. The folding sequences shown in Fig. 3c–f are

examples that demonstrate how small changes in the folding initiation of certain unit cells could prevent collisions. However, many different folding sequences could be employed to achieve the same result, *e.g.* sequences involving variations in the folding speed and the starting time of the unit cells, individual patches, or even individual hinges, thereby offering greater design freedom to ensure collision-free folding. Sequential folding could be physically realized in different ways, *e.g.* using localized external triggers [35] or built-in design features [36].

2.5. Self-folding experiments

We physically realized our self-folding minimal surface structures by attaching stretched elastomer sheets to 3D printed foldable frames (see Section 4). Upon release, the strain energy in the sheets causes the flat polygonal frame to self-fold into the desired skew polygonal configuration, and the sheet spanning the frame adopts an energy-minimizing saddle-shaped geometry, approximating the minimal surface (Fig. 4a). Being a combination of (semi-) rigid beams and flexible sheets, our structures represent a special case of Kirchhoff–Plateau surfaces [37], in which virtually all frame deformation is concentrated at the hinges. The direction of folding of the frame is controlled by the eccentric position of the sheet with respect to the hinge location: the pre-stretched sheet is attached on one side of the frame, while the hinge layer (see Section 4 and Fig. S4) is situated on the other side, ensuring preferential folding in the direction of the side to which the sheet is attached. The level of pre-strain in the elastomer sheets should at least be high enough to accommodate the relative amount of area shrinkage that occurs in the sheet during the folding motion, which varies between approximately 10% and 30% depending on the patch type (Fig. S1b). Moreover, the strain energy stored in the pre-stretched sheets should be high enough to drive the folding motion of the frame, *i.e.* to overcome the bending resistance at the hinges and the gravitational forces acting on the frame, and also to keep the frame in the folded configuration afterwards. During the experiments presented here, the sheets were bi-axially strained by 50% in both directions (see Section 4), which enabled the rapid self-folding of the frame and resulted in ample residual tension in the sheet to maintain the frame in its folded configuration. We assessed the mean (H) curvature profile of the sheet surface on the basis of micro-computed tomography scans of the self-folded patches (see Section 4), finding that H is close to zero everywhere (Fig. 4b). This demonstrates that the self-folded patches adopt a shape very close to the ideal minimal surface, as minimal surfaces are mathematically defined as having $H = 0$ everywhere. While deviations from the ideal minimal surface shape arise as a consequence of, *e.g.*, sheet wrinkling at the hinges, non-uniform sheet straining, and competition between the bending and stretching energies of the finite thickness sheet [38], we demonstrate that a relatively simple combination of rigid and flexible components enables the folding of complex, hyperbolic shapes that are incompatible with traditional origami methods. In addition to individual patches, we also 3D printed unit cell nets of the four TPMS, which were self-folded to the final configuration after attaching and releasing the pre-strained sheet material (Fig. 4c). Since all patches within the same unit cell fold in the same direction, a consequence of using vertex-connections, the sheet is attached to the same side for all patches within the unit cell, which is convenient during fabrication. To demonstrate the self-folding capability of this approach, a time sequence of the self-folding of the CLP unit cell is shown in Fig. 4d (see also SI_Movie8). Upon release, the pre-stretched latex sheet rapidly causes the frame to self-fold, and the built-in stopping mechanisms cause it to stop at the desired configuration (see Section 4). Moreover, we show that attaching unit cell nets together using edge-connections enables the self-folding of larger assemblies (Fig. 4e). As a demonstrative

example, four connected unit cells for the D-surface are shown in Fig. 4e, but this approach is also applicable to larger morphologies as long as collisions during folding are avoided.

3. Discussion

Whereas previous origami-based designs have been restricted to primarily developable geometries, such as polyhedral structures and classical origami tessellations, the presented approach realizes the self-folding of previously unfoldable, non-developable, TPMS structures through the rational design of foldable surface patches and their connections. While we focused here on four TPMS types, other spanning minimal surfaces could also be constructed, if a suitable flattening of the skew polygonal patch is found. By elucidating the folding kinematics of the four types of generating patches, and by connecting multiple patches using either vertex- or edge-connections, a large variety of foldable 3D morphologies could be generated that are all a portion of the infinite minimal surface. Our focus has been on generating 2D nets by first constructing unit cells, using vertex-connections, and connecting unit cells together using edge-connections. However, many different foldable 2D nets could be generated, *e.g.* to fold periodic layers of TPMS unit cells that could be stacked to assemble arbitrarily large portions of the TPMS (see SI). The relatively simple folding "rules" of our approach, capable of describing complex folding motions, could potentially benefit from efficient optimization algorithms to uncover foldable nets for specific TPMS morphologies. Due to the complexity of the TPMS morphologies, a key challenge in the further development of the presented origami approach is the ability to accurately control the folding motion, *i.e.* not only the temporal aspect but also the final configuration, as well as finding ways to lock the structure once folded. The presented approach offers new and exciting perspectives in the development of metamaterials, due to regained access to the flat starting surface. We envision not only origami biosystem applications [39], *e.g.* biomimetic tissue engineering scaffolds with osteogenic and bactericidal surface nano-patterns, but also bi-continuous membranes for fluid transfer with tailored wettability (*e.g.*, self-cleaning membranes) or TPMS-based structures with embedded electronic components. In this work, we focused on sheet-based structures, but beam-based lattices derived from the boundary frames could also be folded. Finally, our approach is not strictly bound by a specific length scale, meaning that it could also inspire the self-folding of architectural-scale tensile structures, nor is it limited to specific constituent materials, as long as a sufficient area distortion of the sheet surfaces and the rigidity of the boundary frames can be obtained.

4. Materials and methods

4.1. Patch kinematics

The folding kinematics of the straight-edged TPMS patches were implemented in Matlab (Mathworks, USA) by calculating the Cartesian coordinates of the vertices as a function of the fold angle θ, from zero until the final folded configuration. The vertex coordinates in the folded configurations were obtained from Fisher and Koch [27]. By calculating the difference between the internal angle sum in the folded, $\sum_i \alpha_i^s$, and flat, $\sum_i \alpha_i^f$, configurations, the required amount of angular change for unfolding was obtained for every hinge vertex. For n hinged vertices, the angular change that needs to be accommodated for every hinge by the folding/unfolding is therefore given as:

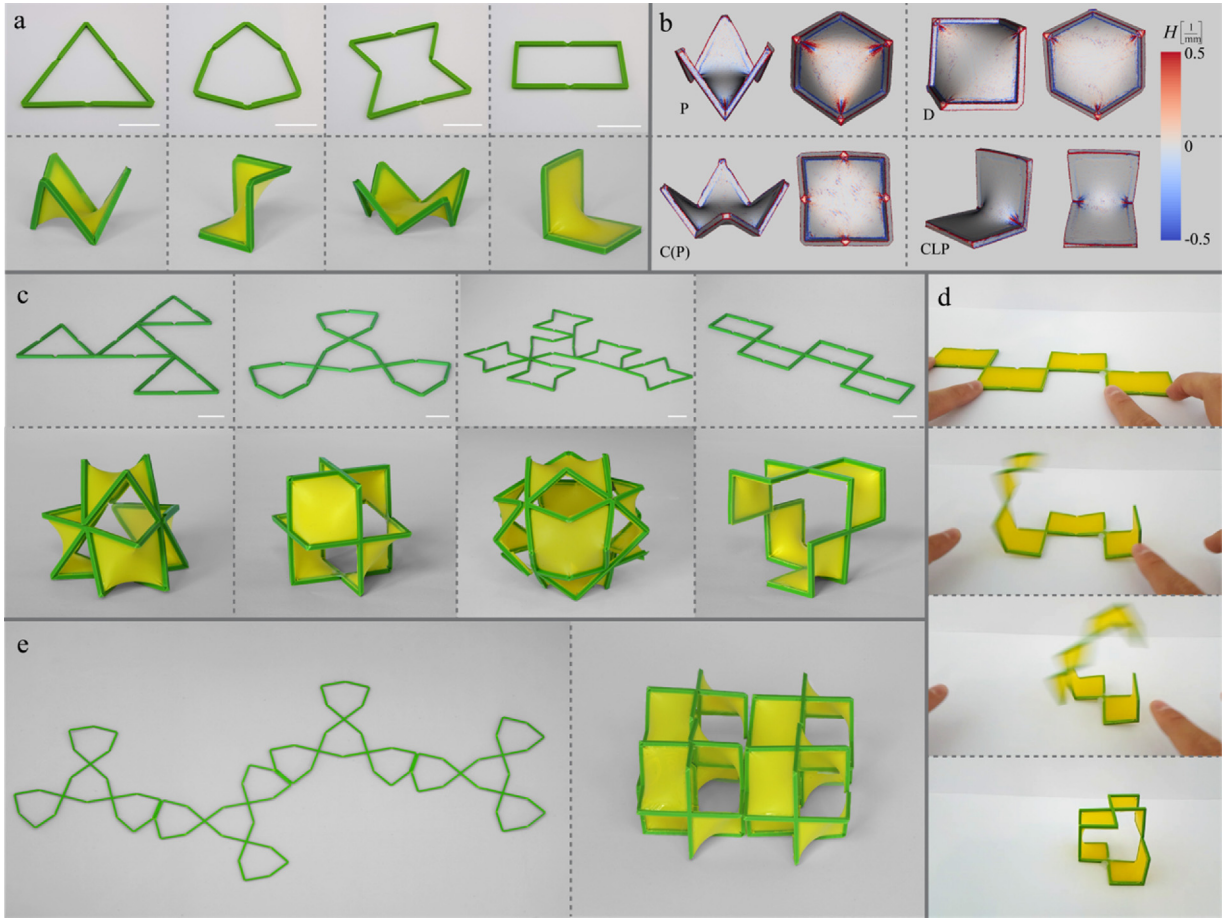$$\Delta \alpha_n \frac{(\sum_i \alpha_i^f - \sum_i \alpha_i^s)}{n}$$

Fig. 4. Self-folded physical models. (a) 3D-printed foldable frames for the four patch types in flat (top row) and folded (bottom row) configurations after the stretched latex sheets have been attached (see Section 4). (b) The mean curvature estimated using the 3D reconstructions of the four patch types obtained from micro-computed tomography data (see Section 4 and SI_Movie7 for more information). (c) 3D-printed foldable TPMS unit cells in the flat (top row) and folded (bottom row) configurations. (d) The self-folding of the CLP unit cell through the pre-tension present in the latex sheet (see SI_Movie8). (e) An assembly of four D unit cells in the flat (left) and folded (right) configurations. All scale bars are 20 mm.

The final fold angle was calculated using the trigonometric relations that were obtained for the folding motion and by considering the orthogonal projection of the skew polygonal patch. As mentioned in the main text, the bowtie patch for the C(P) surface required the in-plane sliding of the hinge vertices. This is illustrated in the Fig. S1a, where δ_1 and δ_2 represent the amount of in-plane sliding of the two pairs of opposite hinge vertices to accommodate the folding. These distances are given by:

$$\delta_1 = l\left(\cos\left(\frac{\pi}{6}\right) - \cos\left(\frac{\pi}{12}\right) + \sin\left(\frac{\pi}{12}\right)\right) = \frac{l}{2}(\sqrt{3} - \sqrt{2})$$

$$\delta_2 = l\left(\cos\left(\frac{\pi}{12}\right) - \sin\left(\frac{\pi}{12}\right) + \sin\left(\frac{\pi}{6}\right) - 1\right) = l\left(\frac{1}{\sqrt{2}} - \frac{1}{2}\right)$$

4.2. Minimal surface generation

The widely-used (and freely available) Surface Evolver software [40] was used to find the minimal surface spanning a given boundary frame. The software numerically finds the minimal surface by minimizing the surface energy using a gradient descent method. Using Matlab, the input files for every desired fold angle were generated, containing the vertex coordinates and the edge numbers of the boundary frame. The surface was then evolved using two consecutive gradient descent and mesh refinement steps, supplemented with equiangulation and vertex averaging, until area convergence was achieved. The resulting minimal surface morphologies were then exported as .obj files and were rendered in KeyShot 5 (Luxion, USA). As described in the main text, the folding motion of the frame entails an area distortion of the surface spanning the frame. This is illustrated in Fig. S1b, showing the evolution of the normalized surface area A/A_0 during folding, obtained by finding the minimal surface spanning the frames at every folding step using the Surface Evolver software.

4.3. Folding kinematics tool

A Matlab tool was developed to explore the folding of user-defined 2D nets consisting of flat patches connected together using either vertex- or edge-connections. By employing the symmetry properties that both types of connections entail (see the main text), the vertex coordinates of every patch in the net could be determined for every fold angle from the initial patch, by using appropriate rotation matrices and translation vectors. For example, copying the initial patch along one of its edges requires rotating the coordinates by angle π around that edge (Fig. S2). Thus, for both edge-connected patches in Fig. S2, the coordinates of a vertex in the copied patch $\boldsymbol{q_i}$ are related to the coordinates of the corresponding vertex in the original patch $\boldsymbol{p_i}$ by:

$$\boldsymbol{q_i} = \boldsymbol{R}(\pi) \cdot \boldsymbol{p_i} + \boldsymbol{t}$$

where $R(\theta)$ is the rotation matrix for a rotation of angle θ about the unit vector $\hat{r} = \frac{r}{\|r\|}$ and is given as (32):

$$R(\theta) = \begin{pmatrix} \cos(\theta) + \hat{r}_x^2(1 - \cos(\theta)) & \hat{r}_x\hat{r}_y(1 - \cos(\theta)) - \hat{r}_z\sin(\theta) & \hat{r}_x\hat{r}_z(1 - \cos(\theta)) - \hat{r}_y\sin(\theta) \\ \hat{r}_x\hat{r}_y(1 - \cos(\theta)) - \hat{r}_z\sin(\theta) & \cos(\theta) + \hat{r}_y^2(1 - \cos(\theta)) & \hat{r}_y\hat{r}_z(1 - \cos(\theta)) - \hat{r}_z\sin(\theta) \\ \hat{r}_x\hat{r}_z(1 - \cos(\theta)) - \hat{r}_y\sin(\theta) & \hat{r}_y\hat{r}_z(1 - \cos(\theta)) - \hat{r}_x\sin(\theta) & \cos(\theta) + \hat{r}_z^2(1 - \cos(\theta)) \end{pmatrix}$$

The vector t represents a translation to ensure that the original patch and its rotated copy are connected at the desired vertex. For example, for an edge-connection about the edge defined by points p_1 and p_2 (Fig. S2), the translation vector is given by:

$$t = p_2 - R(\pi) \cdot p_2$$

We verified the absence of coinciding patches in the folded configurations by checking for duplicate coordinates in the total coordinate matrix. The folding sequences for multiple-unit assemblies were visually examined for patch collisions after the minimal surfaces were added to the boundary frames in Surface Evolver. To avoid collisions, sequential folding was implemented by using multiple fold angle variables θ_i that increase at the same rate but start at different times. Fig. S3 shows two edge-connected P unit cells that were folded according to different θ, showing that one unit is essentially a "time-shifted" copy of the other, i.e.

$$\theta_a = \theta_b - \delta_t$$

where δ_t represents the time shift and can be positive or negative.

4.4. Design of foldable frames

Foldable patch and unit cell frames were designed in Solid-Works 2016 (Dassault Systèmes, France). The frame edges, which are supposed to behave rigidly, were given a square 2 mm × 2 mm cross-section, while the hinges were designed as a 0.3 mm layer connecting the rigid edges and facilitating the folding motion through local bending. This hinge design enabled efficient folding yet simple fabrication. At the location of the hinges, the frame edges were given a chamfer such that the folding of the frame would be halted at the desired fold angle (Fig. S4).

4.5. 3D printing

The frames were 3D printed on an Ultimaker 2+ FDM printer (Ultimaker, The Netherlands) using poly-lactic acid (PLA) filaments with a 0.25 mm diameter nozzle and a layer thickness of 0.6 mm. In the case of the C(P) surface, a flat 'star' patch (see SI text) was printed, which was manually deformed into the bow-tie configuration after printing to enable the in-plane sliding of the hinge vertices upon folding. Latex sheets (150 μm thick, TheraBand, USA) were bi-axially stretched ($\varepsilon_1 = \varepsilon_2 \approx 0.5$) and fixed to a cutting board. The flat frames were adhesively bonded to the stretched latex sheets using a cyanoacrylate adhesive (Bison, The Netherlands) and were cured at room temperature. Next, the latex sheet was cut along the outside boundary of the frame, thereby only retaining the stretched latex spanning the frame. The frame was then released from the cutting board and was allowed to self-fold into the final configuration.

4.6. Micro-computed tomography and curvature estimation

Micro-computed tomography (μ-CT) images of four 3D printed self-folded patches (one from each type of the minimal surfaces considered here) were acquired using a Phoenix Nanotom scanner (General Electric, USA). Tomographic reconstructions were made with a slice increment of 22.5 μm, and a matrix of 2284 × 2284 pixels. The voxel size of the volumetric data was

22.5 μm × 22.5 μm × 22.5 μm. As the resulting size of the volumetric datasets was too large (over 20 GB) to be opened by any image analysis software package (e.g., 3D slicer, Fiji) on a desktop computer with Intel(R) Xen(R) E5-2687W (2 cores) at 3.40 GHz and 64.0 GB RAM, each 3D volumetric intensity image was resized by a factor of 0.4 using the function "imresize3" available in Matlab (Mathworks, USA). Subsequently, each volumetric dataset with a voxel size of 56 μm × 56 μm × 56 μm was post-processed using Mimics (version 14.01, Materialise, Belgium). Using this software, all patches were segmented and 3D models were reconstructed based on the segmentation results. During the reconstruction, the smoothing function available in Mimics was applied with a smoothing factor of 1.0. To ensure proper definition of the contour of the patches, smoothing effects were visually examined. Using the same software, 3D models were exported as STL files. The mean curvature of each triangulated patch surface (.STL) was estimated using the "vtkCurvatures" class of The Visualisation Tookit (VTK) in Python [41].

Data availability

All data used to generate these results is available in the main text or supplementary material. The codes could be obtained from the corresponding author upon request.

Appendix A. Supplementary data

Supplementary data associated with this article can be found, in the online version, at doi:10.1016/j.apmt.2019.03.007.

References

[1] S. Hyde, et al., The Language of Shape: The Role of Curvature in Condensed Matter: Physics, Chemistry and Biology, Elsevier Science, Amsterdam, The Netherlands, 1996.
[2] H.A. Schwarz, Gesammelte mathematische abhandlungen, Springer, Berlin, 1890.
[3] L. Han, S. Che, Adv. Mater 30 (17) (2018) 1705708.
[4] R. Lipowsky, Nature 349 (6309) (1991) 475.
[5] V. Saranathan, et al., Proc. Natl. Acad. Sci. USA 107 (26) (2010) 11676.
[6] S.C. Kapfer, et al., Biomaterials 32 (29) (2011) 6875.
[7] F.S.L. Bobbert, et al., Acta Biomater. 53 (2017) 572.
[8] S.B. Blanquer, et al., Biofabrication 9 (2) (2017) 025001.
[9] M.D. Turner, et al., Nat. Photonics 7 (10) (2013) 801.
[10] O. Al-Ketan, et al., Adv. Mater. Technol. 2 (2) (2016) 1600235.
[11] W. Lee, et al., Sci. Rep. 6 (2016) 20312.
[12] N. Thomas, et al., Desalination 443 (2018) 256.
[13] M.L. Brongersma, et al., Nat. Mater. 13 (5) (2014) 451.
[14] T.L. Liu, C.-J.C. Kim, Science 346 (6213) (2014) 1096.

[15] S. Dobbenga, et al., Acta Biomater. 46 (2016) 3.
[16] A. Elbourne, et al., J. Colloid Interface Sci. 508 (2017) 603.
[17] X. Zang, et al., Adv. Mater. (2018) 1800062.
[18] S. Janbaz, et al., Sci. Adv. 3 (11) (2017).
[19] S.J.P. Callens, A.A. Zadpoor, Mater. Today 21 (3) (2018) 241.
[20] R. Sawhney, K. Crane, ACM Trans. Graph. (TOG) 37 (1) (2017) 5.
[21] J. Kim, et al., Science 335 (6073) (2012) 1201.
[22] H. Aharoni, et al., Proc. Natl. Acad. Sci. USA (2018) 201804702.
[23] W.M. van Rees, et al., Proc. Natl. Acad. Sci. USA (2017).
[24] T. Castle, et al., Interface Focus 2 (5) (2012) 555.
[25] J.F. Sadoc, J. Charvolin, Acta Crystallogr. Sect. A 45 (1) (1989) 10.
[26] S. Hyde, S. Andersson, Z. Kristallogr. – Cryst. Mater. 168 (1–4) (1984) 221.
[27] W. Fischer, E. Koch, Philos. Trans. R. Soc. Lond. A: Math. Phys. Eng. Sci. 354 (1715) (1996) 2105.
[28] E.A. Lord, Colloids Surf. A: Physicochem. Eng. Aspects 129 (1997) 279.
[29] E.D. Demaine, J. O'Rourke, Geometric Folding Algorithms: Linkages, Origami, Polyhedra, Cambridge University Press, 2008.
[30] D. Hilbert, S. Cohn-Vossen, Geometry and the Imagination, Chelsea Publishing Company, New York, USA, 1990.
[31] T. Castle, et al., Phys. Rev. Lett. 113 (24) (2014) 245502.
[32] A.H. Schoen, Interface Focus 2 (5) (2012) 658.
[33] E. Koch, W. Fischer, Z. Kristallogr. – Cryst. Mater. 183 (1–4) (1988) 129.
[34] J. Cui, et al., Adv. Funct. Mater. (2018) 1802768.
[35] S.M. Felton, et al., Soft Matter 9 (32) (2013) 7688.
[36] X. Hu, et al., Nat. Commun. 7 (2016) 12919.
[37] L. Giomi, L. Mahadevan, Proc. R. Soc. A 468 (2143) (2012) 1851.
[38] E. Sharon, E. Efrati, Soft Matter 6 (22) (2010) 5693.
[39] V.A. Bolaños Quiñones, et al., Adv. Biosyst. (2018) 1800230.
[40] K.A. Brakke, Exp. Math. 1 (2) (1992) 141.
[41] vtk.org, vtkCurvatures Class Reference, 2018.